Effect of lift force and hydrodynamic torque on fluidisation of non-spherical particles

Mema, Ivan; Mahajan, Vinay V.; Fitzgerald, Barry W.; Padding, Johan T.

Important note
To cite this publication, please use the final published version (if applicable).
Please check the document version above.

Effect of lift force and hydrodynamic torque on fluidisation of non-spherical particles

Ivan Mema, Vinay V. Mahajan, Barry W. Fitzgerald, Johan T. Padding *

Intensified Reaction and Separation Systems, Department of Process and Energy, Delft University of Technology, Leeghwaterstraat 39, 2628 CB Delft, The Netherlands

HIGHLIGHTS

- CFD-DEM simulations of spherocylindrical particles in a fluidised bed.
- Explore the effect of varying hydrodynamic force conditions.
- Lift and torque correlations derived from recent DNS simulations are used.
- Lift has considerable influence on the velocity of particles parallel to fluid flow.
- Inclusion of hydrodynamic torque greatly affects preferred orientation of particles.

GRAPHICAL ABSTRACT
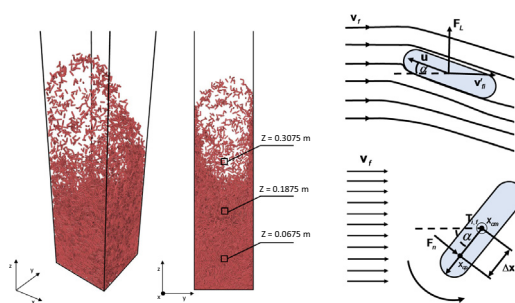
ABSTRACT

The aim of many industrial processes is to manipulate solid particle aggregates within gas suspensions. Prime examples of such processes include fluidised bed reactors, cyclone separators, and dust collectors. In recent years, fluidised bed reactors have been used in the gasification of biomass particles. When fluidised, these particles are subject to various hydrodynamic forces such as drag, lift and torque due to interactions with the fluid. Computational approaches, which can be used to replicate laboratory and industrial scale processes, offer a crucial method for the study of reactor design and for the formulation of optimal operating procedures. Until now, many computer models have assumed particles to be spherical whereas, in reality, biomass feedstocks typically consist of non-spherical particles. While lift and torque are of minimal importance for spherical particles, non-spherical particles experience varying lift force and torque conditions, depending on particle orientation relative to the direction of the fluid velocity. In this study, we present a numerical investigation on the effect of different lift force and torque correlations on fluidised spherocylindrical particles. We find that lift force has a significant influence on particle velocities parallel to the direction of gravity. On the other hand, particle orientation is dependent on hydrodynamic torque. Results from this numerical study provide new insight with regards to the dynamics of non-spherical particles that can be of paramount importance for industrial processes involving non-spherical particles.

© 2018 The Authors. Published by Elsevier Ltd. This is an open access article under the CC BY-NC-ND license (http://creativecommons.org/licenses/by-nc-nd/4.0/).

1. Introduction

Many industrial processes such as fluidised bed reactors, cyclone separators, dust collectors, and pulverised-coal combustors involve the processing of dense gas-solid flows. These devices

are categorised as gas-solid contactors, of which the fluidised bed reactor is a proto-typical example (Werther, 2000; Warnecke, 2000; Grace et al., 1997; Mahajan et al., 2018a). Due to their favourable mass and heat transfer characteristics, gas-fluidised beds are utilised in a number of industries such as the chemical (Son and Kim, 2006; Mattisson et al., 2018), petrochemical (Williams and Williams, 1999; Xue et al., 2016) and energy industries (Nikoo and Mahinpey, 2008; Chen et al., 2017). In addition, fluidised bed reactors are used in large-scale operations involving the granulation, drying and synthesis of fuels, base chemicals and polymers (Grace et al., 1997). In recent years, there has been increased application of fluidised beds in biomass gasification (McKendry, 2002; Bridgwater, 2003, 2006; Alauddin et al., 2010) using a variety of raw materials such as rice husks (Cai et al., 2018), cooking oil (Chen et al., 2017) and willow (Woytiuk et al., 2017). Hence, the prediction of the response of dense gas-solid flows in fluidised reactors via computational investigation is highly important for both reactor design and the determination of optimal operating conditions for a variety of important applications. However, simulations of dense gas-solid flows generally represent the solid phase as perfect spherical entities whereas, in reality, the solid biomass phase is composed of discrete particles of varying non-spherical geometries (Kruggel-Emden and Vollmari, 2016; Gil et al., 2014; Mahajan et al., 2017, 2018a; Vorobiev et al., 2017).

Describing non-spherical particles in simulations can give rise to a variety of issues. While spheres can be described by a single parameter, i.e. diameter, non-spherical particles require more parameters. Even regular non-spherical shapes, such as ellipsoids or spherocylindrical particles, require at least two parameters to account for their geometry. For highly irregular particle shapes, the computational demands with regards to the detection of particle-particle interactions, and the calculation of resulting contact forces, drastically increase. An additional concern is the determination of the hydrodynamic forces and torques acting on particles due to the fluid flow. For non-spherical particles, the hydrodynamic forces, such as drag, transverse lift and pitching torque, can vary appreciably with particle orientation, and thus crucially dictate the translational motion of particles. Pitching torque is generated when the centre of pressure associated with the total aerodynamic force does not act through the centre of mass of a specific particle. Drag force, lift force, and pitching torque can be characterised by dimensionless coefficients that depend on particle velocity and orientation relative to the flow as well as the Reynolds number (Re). A number of drag force coefficients for non-spherical particles are available in the literature (Tran-Cong et al., 2004; Loth, 2008; Hölzer and Sommerfeld, 2008, 2009; Sanjeevi and Padding, 2017; Sanjeevi et al., 2018) while, recently, lift coefficient correlations (Zastawny et al., 2012; Richter and Nikrityuk, 2013; Ouchene et al., 2015, 2016; Sanjeevi et al., 2018) and torque coefficient correlations (Zastawny et al., 2012; Sanjeevi et al., 2018) have also been defined for non-spherical particles.

For a dilute particle suspension and depending on the Reynolds number, the lift force can be more than half the drag force for non-spherical particles in a gas flow (Mandø and Rosendahl, 2010). As a result, lift can significantly influence the trajectory of non-spherical particles (Richter and Nikrityuk, 2013; Sanjeevi and Padding, 2017; Sanjeevi et al., 2018). However, it is not clear how lift force will affect non-spherical particles in dense systems such as those encountered in dense gas-fluidised systems. Similarly, the effect and importance of pitching torque on non-spherical particles under fluidised conditions is also poorly understood. In this paper, we present a preliminary investigation on the effect of varying lift and torque conditions on non-spherical particles, specifically spherocylindrical particles, in a laboratory scale gas-fluidised bed reactor. We employ a series of lift and torque correlations that have been derived for single isolated particles (Zastawny et al., 2012; Sanjeevi and Padding, 2017; Sanjeevi et al., 2018) as an initial approximation of the lift and torque experienced by spherocylindrical particles during fluidisation. We present results on the relevance of varying lift and pitching torque conditions for spherocylindrical particles by studying particle dynamics, velocity profiles, particle orientations, and angular momentum in a reactor.

This paper is arranged as follows. We will first outline the CFD-DEM numerical model used in this study focusing on the implementation of contact detection, drag forces, lift forces, and pitching torque for spherocylindrical particles (Section 2). Thereafter we present the simulation parameters for this study in Section 3. In Section 4, we explore the effect of varying lift and torque conditions in dense fluidised beds. Finally, we draw conclusions from this study and provide an outlook for future investigations.

2. Numerical approach

For this study we implement the CFD-DEM algorithm to simulate a coupled particle-fluid system, which has been extensively employed to simulate systems where particle-fluid interactions are relevant (Tsuji et al., 1993; Zhu et al., 2007, 2008; Deen et al., 2007; Zhao and Shan, 2013; Salikov et al., 2015; Mahajan et al., 2017). The CFD component of the algorithm is solved using the Open Source package OpenFOAM while the DEM component is implemented using LIGGGHTS, which stands for LAMMPS Improved for General Granular and Granular Heat Transfer Simulations, and is an Open Source package for modelling granular material via the discrete element method (DEM). Coupling of the CFD and DEM components is facilitated by the Open Source coupling engine CFDEM, which executes both the DEM solver and CFD solver consecutively. The CFDEM engine allows for execution of the program for a predefined number of time steps after which data is exchanged between the OpenFOAM solver and LIGGGHTS solver (Kloss et al., 2012). In this study, the Open Source codes have been adapted for the implementation of spherocylindrical particles and further details on the CFD-DEM approach can be found in the paper of Mahajan et al. (2018b).

2.1. Discrete Element Method (DEM)

To simulate interactions between the solid spherocylindrical particles we use the discrete element method (DEM), a soft contact model first introduced by Cundall and Strack (1979) to describe interactions between granular particles (Cundall and Strack, 1979). The simplest DEM contact model approximates grains as either disks in 2D or spheres in 3D, an approach that is sufficient to replicate laboratory-scale force chains (Aharonov and Sparks, 1999, 2002) and depict percolation-like contact networks (Fitzgerald et al., 2014). In DEM, the trajectory of each particle is numerically integrated over time and subject to local contact forces and torques. Inter-particle forces develop only when particles spatially overlap.

We have adapted the DEM model to describe the interaction of spherocylinders with rotational and translational degrees of freedom. Consider a spherocylinder particle i in a dense gas-fluidised reactor. The translational motion for spherocylinder i can be calculated by integrating the expression

$$m_i \frac{d\mathbf{v}_i}{dt} = \sum_j \left(\mathbf{F}_{ij,n} + \mathbf{F}_{ij,t} \right) + \mathbf{F}_{i,f} + \mathbf{F}_{i,p} + \mathbf{F}_{i,b} \quad (1)$$

where the sum runs over all neighbours j in contact with particle i, $\mathbf{F}_{ij,n}$ is the normal contact force acting on particle i due to its interaction with particle j, $\mathbf{F}_{ij,t}$ is the tangential contact force acting on particle i due to its interaction with particle j, $\mathbf{F}_{i,f}$ is the total hydro-

dynamic force acting on the particle, $\mathbf{F}_{i,p}$ represents the pressure gradient (buoyancy) force acting on the particle, and $\mathbf{F}_{i,b}$ is the body force acting on the particle including gravity. Further details on the hydrodynamic forces acting on the particle are presented in the next section. The rotational motion of a particle i can be solved using

$$\frac{d(\mathbf{I}_i \cdot \boldsymbol{\omega}_i)}{dt} = \sum_j \mathbf{T}_{ij} + \mathbf{T}_{i,f} \tag{2}$$

where $\mathbf{I}_i$ is the particle moment of inertia tensor, $\boldsymbol{\omega}_i$ is the angular velocity of the particle, $\mathbf{T}_{ij}$ is the contact torque acting on the particle i due to its interaction with neighbouring particle j, and $\mathbf{T}_{i,f}$ is the fluid-induced pitching torque. Note that for spherical particles, the contact torque $\mathbf{T}_{ij}$ is only caused by tangential contact forces. However, for non-spherical particles the torque is caused by *both* tangential and normal contact forces. Particle orientations are described by quaternions in the algorithm. For this study the equations of motion are integrated using the Velocity Verlet method.

Fig. 1 shows an example of an overlapping contact between two spherocylinder particles P_1 and P_2. The identification of contacts between spherocylindrical particles, and the subsequent calculation of the overlap region, is more complicated than in the case of spheres. Two adjacent spherocylindrical particles are deemed to be overlapping once the distance between their shafts is smaller than the sum of their radii. For particle P_i, R is the characteristic radius or radius of the spherical part of the spherocylinder, $\mathbf{r}_i$ is the centre of mass, l is the shaft length, L is the total length, $\mathbf{u}_i$ is the orientation unit vector originating at $\mathbf{r}_i$ and $\mathbf{v}_i$ is the translational velocity. Two spherocylindrical particles are deemed to be in contact when the shortest distance between the central axes is less than the sum of the particle radii i.e. $|\mathbf{s}_2 - \mathbf{s}_1| < 2R$ where $\mathbf{s}_1$ and $\mathbf{s}_2$ are points on the central axes of P_1 and P_2 respectively. The mid-point between $\mathbf{s}_1$ and $\mathbf{s}_2$ is the contact point $\mathbf{r}_c$, the degree of overlapping distance between the particles is δ_n, and $\mathbf{n}_{12}$ and $\mathbf{t}_{12}$ are the normal and tangential unit vectors for the contact respectively. A spherocylinder contact detection algorithm originally developed for granular flows has been used in this study (Vega and Lago, 1994; Pournin et al., 2005; Azéma and Radjaï, 2012; Marschall and Teitel, 2018).

To calculate the normal contact force exerted on particle P_1 by particle P_2, we use a linear spring-dashpot model such that the normal contact force is given by

$$\mathbf{F}_{12,n} = -k_n \delta_n \boldsymbol{n}_{12} - \eta_n \mathbf{v}_{12,n} \tag{3}$$

where k_n is the normal spring constant, η_n is the normal damping coefficient, and $\mathbf{v}_{12,n}$ is the normal relative velocity between the particles. As shown in Eq. (3), the normal contact force is dependent on the degree of overlapping distance δ_n, which is calculated with the aforementioned collision detection scheme for spherocylinders. Using the degree of overlapping or penetrating volume instead of overlapping distance can lead to a better resolution of the normal and tangential forces (Kumar et al., 2018). In addition, when the overlap distance is used for the normal contact force, the volume of the overlap region is effectively ignored and particle volume is not conserved. This can have ramifications for the calculation of local volume fraction, and thus affect the calculation of the coupling between the solid and fluid phases. To overcome this issue, the volume of the overlapping region can be redistributed over the remaining surface of the particle, as demonstrated for spherical particles (Haustein et al., 2017). This issues are prevalent for more detailed, pure granular studies and in dense and compact granular configurations. However, as we aim to study the fluidisation of spherocylinder particles above the minimum fluidisation velocity, persistent compact particle domains are unlikely with particles more likely to be airborne and briefly contacting a smaller number of particles. Hence, we use a simplified approach based upon overlapping distance without accounting for overlapping volume as an approximation. The tangential contact force is calculated from the Coulomb-type friction expression

$$\mathbf{F}_{12,t} = \min(|-k_t \delta_t \boldsymbol{t}_{12} - \eta_t \mathbf{v}_{12,t}|, -\mu |\mathbf{F}_{12,n}|). \tag{4}$$

In this expression k_t, δ_t, η_t, μ, and $\mathbf{v}_{12,t}$ are the tangential spring constant, tangential overlap, tangential damping coefficient, friction coefficient, and tangential relative velocity respectively. δ_t is calcu-
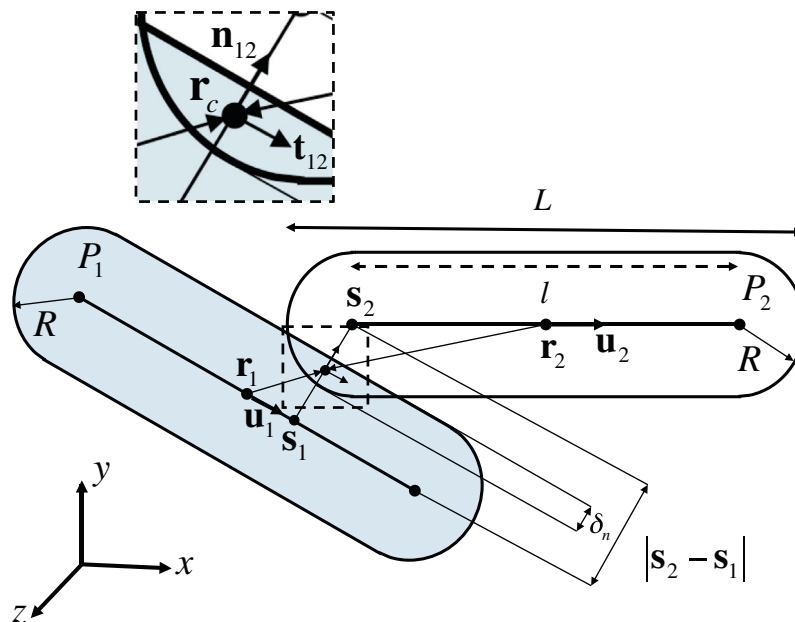

Fig. 1. A schematic of a sample contact between two spherocylinders with each having a shaft length l, a total length L, and a characteristic radius R. The inset image shows details of the normal and tangential unit vectors at the contact.

lated from the time integral of the tangential relative velocity since the development of the initial particle contact and given by

$$\delta_t = \int_{t_{c,0}}^{t} \mathbf{v}_{12,t} dt \tag{5}$$

where $t_{c,0}$ is the time of initial contact between the particles. This expression represents the elastic tangential deformation of the particles since the onset of particle contact. Interactions between the walls and particles are also modelled using the linear spring-dashpot approach of Eq. (3) with the tangential expression given by Eq. (4). Rolling friction for particle-particle and particle-wall interactions is included in the model with the coefficient of rolling friction given in Table 2. Further details on the implementation of rolling friction are available in our previous paper (Mahajan et al., 2018b).

2.2. Computational Fluid Dynamics (CFD)

In CFD-DEM, the fluid is treated as a continuum in which fluid flow features such as boundary layers or vortex shedding are not resolved. Instead, their effects are included through correlations of drag and lift forces. The fluid phase is described on the basis of the volume-averaged Navier-Stokes equations, which are discretised on a uniform grid, and fluid calculations are based upon the standard k-ϵ turbulence model. The equation of continuity is given by

$$\frac{\partial(\epsilon_f \rho_f)}{\partial t} + \nabla \cdot (\epsilon_f \rho_f \mathbf{v}_f) = 0 \tag{6}$$

where ϵ_f is the fluid volume fraction, ρ_f is the fluid density, and $\mathbf{v}_f$ is the fluid velocity. The expression for momentum conservation is given as

$$\frac{\partial(\epsilon_f \rho_f \mathbf{v}_f)}{\partial t} + \nabla \cdot (\epsilon_f \rho_f \mathbf{v}_f \mathbf{v}_f) = -\epsilon_f \nabla p + \nabla \cdot (\epsilon_f \tau_f) + \mathbf{R}_{f,p} + \epsilon_f \rho_f \mathbf{g} \tag{7}$$

where τ_f is the stress tensor for the fluid phase, $\mathbf{g}$ is gravity, and $\mathbf{R}_{f,p}$ represents the momentum exchange between the fluid and particle phase. The latter is obtained by distributing the particle interactions with the fluid phase using the following expression (Xu and Yu, 1997)

$$\mathbf{R}_{f,p} = -\frac{\sum_{p=1}^{N_p}(\mathbf{F_D^p} + \mathbf{F_L^p})}{V_{\text{cell}}} \tag{8}$$

where p is the particle label, N_p is the number of particles in the computational fluid cell, $\mathbf{F}_D^p$ is the drag force acting on particle p due to the fluid, $\mathbf{F}_L^p$ is the lift force acting on particle p due to the fluid, and V_{cell} is the volume of the computational fluid cell. We do not consider two-way coupling of the torque since it has negligible localized effects on the fluid. Expressions for the hydrodynamic forces are outlined in the proceeding sections.

2.2.1. Drag force

The drag force on a single particle $\mathbf{F}_{D0}$, in the absence of neighbouring particles, acts in the direction of the relative velocity between fluid and particle and is expressed as

$$\mathbf{F}_{D0} = \frac{1}{2} C_D \rho_f \frac{\pi}{4} d_p^2 |\mathbf{v}_f - \mathbf{v}_i| (\mathbf{v}_f - \mathbf{v}_i) \tag{9}$$

where C_D is the drag coefficient, d_p is the particle volume equivalent diameter or the diameter of a sphere with the same volume as the spherocylinder, $\mathbf{v}_f$ is the fluid velocity interpolated to the location of particle i, and $\mathbf{v}_i$ is the velocity of particle i. A number of drag correlations have been developed in the past that account for particle shape (Rosendahl, 2000; Loth, 2008; Hölzer and Sommerfeld,

2008; Zastawny et al., 2012; Richter and Nikrityuk, 2013; Ouchene et al., 2016). In this study, as an approximation, we employ the drag force correlation for arbitrary shaped particles established by Hölzer and Sommerfeld (2008)

$$C_D = \frac{8}{Re_p}\frac{1}{\sqrt{\Phi_\parallel}} + \frac{16}{Re_p}\frac{1}{\sqrt{\Phi}} + \frac{3}{\sqrt{Re_p}}\frac{1}{\Phi^{3/4}} + 0.42 \times 10^{0.4(-\log\Phi)^{0.2}}\frac{1}{\Phi_\perp} \tag{10}$$

where Re_p is the particle Reynolds number given by $Re_p = \rho_f d_p |\mathbf{v}_f - \mathbf{v}_i|/\mu_f$ where μ_f is the fluid viscosity, Φ is the particle sphericity, $\Phi_\parallel$ is the lengthwise sphericity, and $\Phi_\perp$ is the crosswise sphericity. Besides being universally applicable to different shapes and easy to implement, this expression is quite accurate given that it has a mean relative deviation from experimental data of only 14.1%, significantly lower than previous expressions (Haider and Levenspiel, 1989; Ganser, 1993).

In a dense gas-fluidised system the drag force acting on a given particle will be affected by neighbouring particles. To account for this effect, we implement the Di Felice modified drag force expression (Felice, 1994), which was originally derived for spherical particles and is applied here as an approximation for the effect of neighbouring non-spherical particles on the drag force experienced by a non-spherical particle

$$\mathbf{F}_D = \frac{1}{2} C_D \rho_f \epsilon_f^{2-\chi} \frac{\pi}{4} d_p^2 |\mathbf{v}_f - \mathbf{v}_i| (\mathbf{v}_f - \mathbf{v}_i) \tag{11}$$

where χ is a correction factor given by

$$\chi = 3.7 - 0.65 \exp\left[(-(1.5 - \log(Re_p))^2/2\right] \tag{12}$$

where the particle Reynolds number Re_p is calculated using the expression previously defined. A revision of the Di Felice model by Rong et al. (2013) accounts for the effect of porosity and Re_p on χ. However, in our previous study (Mahajan et al., 2018b), we concluded that this extension demonstrated similar behaviours to the Di Felice model. Therefore, we do not consider the expressions of Rong et al. in this study.

2.2.2. Lift force

For non-spherical particles suspended in a fluid flow, a shape induced lift force, similar to the concept of an aerofoil in aerodynamics, can significantly affect the trajectory of a particle. When the axis of an elongated particle, such as a spherocylindrical particle in this study, is inclined to the direction of relative fluid flow, the flow fields on the upper and lower sides of the particle differ. The pressure drops in regions of rapid flow while the pressure increases in regions where the fluid velocity decreases (Richter and Nikrityuk, 2013), thus leading to an asymmetric pressure distribution and inducing a lift force perpendicular to the direction of relative fluid flow. An example of the lift force $\mathbf{F}_L$ due to a fluid flow for a spherocylinder that is not aligned with the direction of fluid flow is shown in Fig. 2. Here $\mathbf{v}'_{fi}$ is the relative velocity of the fluid with respect to the particle i. The lift force $\mathbf{F}_L$ is orthogonal to $\mathbf{v}'_{fi}$ and, because of symmetry, lies in the plane defined by the particle orientation vector $\mathbf{u}_i$ and $\mathbf{v}'_{fi}$. For spherocylinder particles there is no lift force when the central particle axis is perpendicular to or aligned with the direction of relative fluid flow as there will be no resulting pressure difference. However, arbitrary shaped particles can still be subject to a lift force even when they are aligned with the flow direction, similar to effects observed for a cambered airfoil.

The magnitude of the lift force F_L experienced by an isolated spherocylinder is expressed as

$$F_L = \frac{1}{2} C_L \rho_f \frac{\pi}{4} d_p^2 |\mathbf{v}_f - \mathbf{v}_i|^2 \tag{13}$$
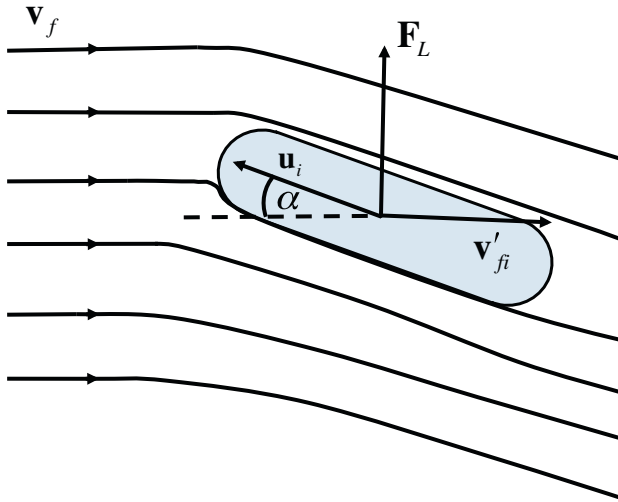
Fig. 2. Lift vector orientation based on the relative velocity of the fluid with respect to the particle $\mathbf{v}'_{fi} = \mathbf{v}_f - \mathbf{v}_i$ and particle orientation vector $\mathbf{u}_i$. The angle of incidence of the fluid flow α is also indicated on the figure.

where C_L is the lift force coefficient. To ensure that the lift force for a particle is correctly oriented, F_L is multiplied by the lift force orientation vector $\hat{\mathbf{e}}_{L_0}$ which is given as

$$\hat{\mathbf{e}}_{L_0} = \frac{\mathbf{u}_i \cdot \mathbf{v}'_{fi}}{\left| \mathbf{u}_i \cdot \mathbf{v}'_{fi} \right|} \frac{(\mathbf{u}_i \times \mathbf{v}'_{fi}) \times \mathbf{v}'_{fi}}{\left\| (\mathbf{u}_i \times \mathbf{v}'_{fi}) \times \mathbf{v}'_{fi} \right\|} \qquad (14)$$

The resultant lift force experienced by a particle is then expressed as $\mathbf{F}_L = F_L \hat{\mathbf{e}}_{L_0}$. For this study we use two lift correlation functions (Zastawny et al., 2012; Sanjeevi et al., 2018), which are presented in Table 1.

In the case of lift force, a dedicated multiparticle correlation is currently unavailable in the literature. Nonetheless, in a preliminary study on the influence of lift force on the dynamics of spherocylinders in a small reactor, we investigated the use of the Di Felice approximation for the calculation of lift force (Mema et al., 2017). While the inclusion of the Di Felice approximation leads to changes in particle dynamics, fundamentally, this expression has been derived specifically for drag forces (Felice, 1994). Therefore, in this study, we do not account for the effect of neighbouring particles on lift force, as is done using the Di Felice correlation for drag force.

Table 1
Table of the lift and torque correlation functions from references Sanjeevi et al. (2018) and Zastawny et al. (2012) used in this study. The fitting coefficients are provided in the Appendix.

	Correlation type	Correlation expression
Zastawny et al. (2012)	Lift	$C_{L,\alpha}^Z = \left(\frac{b_1^Z}{Re^{b_2^Z}} + \frac{b_3^Z}{Re^{b_4^Z}} \right) \sin(\alpha)^{b_5^Z + b_6^Z Re^{b_7^Z}} \cos(\alpha)^{b_8^Z + b_9^Z Re^{b_{10}^Z}}$
Sanjeevi et al. (2018)	Lift	$C_{L,\alpha}^S = \left(\frac{b_1^S}{Re} + \frac{b_2^S}{Re^{b_3^S}} + \frac{b_4^S}{Re^{b_5^S}} \right) \sin(\alpha)^{1 + b_6^S Re^{b_7^S}} \cos(\alpha)^{1 + b_8^S Re^{b_9^S}}$
Zastawny et al. (2012)	Torque	$C_{T,\alpha}^Z = \left(\frac{c_1^Z}{Re^{c_2^Z}} + \frac{c_3^Z}{Re^{c_4^Z}} \right) \sin(\alpha)^{c_5^Z + c_6^Z Re^{c_7^Z}} \cos(\alpha)^{c_8^Z + c_9^Z Re^{c_{10}^Z}}$
Sanjeevi et al. (2018)	Torque	$C_{T,\alpha}^S = \left(\frac{c_1^S}{Re^{c_2^S}} + \frac{c_3^S}{Re^{c_4^S}} \right) \sin(\alpha)^{1 + c_5^S Re^{c_6^S}} \cos(\alpha)^{1 + c_7^S Re^{c_8^S}}$

2.2.3. Hydrodynamic torque

As demonstrated in the preceding sections, drag force acts in the direction of relative fluid flow and depends on particle orientation relative to the flow (Mandø and Rosendahl, 2010), while lift force leads to a force perpendicular to the relative fluid flow (Mema et al., 2017; Zastawny et al., 2012; Ouchene et al., 2016). When the centre of pressure $\mathbf{x}_{cp}$ acting on a non-spherical particle does not coincide with the centre of mass of the particle $\mathbf{x}_{cm}$, a hydrodynamic pitching torque results and acts around the axis perpendicular to the plane of relative fluid velocity $\mathbf{v}'_{fi}$ and particle orientation vector $\mathbf{u}_i$. The torque can change the angle of incidence α of the particle. The development of hydrodynamic torque acting on a spherocylindrical particle is shown in Fig. 3. In the figure the angle of incidence α is defined as the angle between the direction of flow and the unit normal joining x_{cp} and x_{cm}. Note that a particle can also experience rotational torque that acts around the axis of symmetry of the particle. However, we do not include such a rotational torque in this study. For the remainder of this paper pitching torque is referred to as hydrodynamic torque.

There are only a few studies that have previously focused on the formulation of expressions for hydrodynamic torque. While approximate torque expressions have been generated for different non-spherical particle types (Zastawny et al., 2012; Ouchene et al., 2016; Richter and Nikrityuk, 2013; Mandø and Rosendahl, 2010), the most pertinent expression for this study has been recently derived by Sanjeevi et al. (2018) for the exact spherocylindrical particles of this study. Hydrodynamic torque can be calculated using two approaches. First, the hydrodynamic torque can be calculated using $\Delta \mathbf{x}$ (Mandø and Rosendahl, 2010), which is the vector between $\mathbf{x}_{cp}$ and $\mathbf{x}_{cm}$ (Fig. 3), and the normal force $\mathbf{F}_n$ acting through $\mathbf{x}_{cm}$ using the expression

$$\mathbf{T} = \Delta \mathbf{x} \times \mathbf{F}_n. \qquad (15)$$

Here, $\mathbf{F}_n$ is the normal component of the sum of all forces acting at $\mathbf{x}_{cp}$. Using an expression for non-spherical particle torques (Rosendahl, 2000), the magnitude of Δx can be expressed as a function of α by

$$\Delta x = \frac{L}{4}(1 - (\sin \alpha)^3) \qquad (16)$$

where L is the particle length.
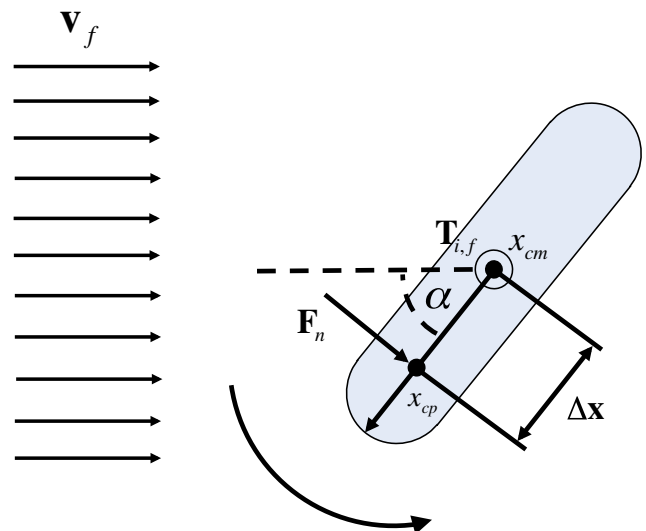
Fig. 3. A spherocylinder subject to torque. The difference between the centre of pressure $\mathbf{x}_{cp}$ and the centre of mass $\mathbf{x}_{cm}$ leads to the development of a hydrodynamic torque $\mathbf{T}_{i,f}$. Δx is the distance between $\mathbf{x}_{cp}$ and $\mathbf{x}_{cm}$.

In this study, we have employed a second approach for the calculation of the hydrodynamic torque acting on an isolated spherocylinder, which uses an expression similar to that used for the calculation of drag (Eq. (9)) and lift (Eq. (13)) and is expressed as

$$T_P = \frac{1}{2} C_T \rho_f \frac{\pi}{8} d_p^3 |\mathbf{v}_f - \mathbf{v}_i|^2 \qquad (17)$$

where C_T is the torque coefficient. The hydrodynamic torque is directed perpendicular to the plane of the particle relative velocity and the particle orientation vector in Fig. 3. Hence, the torque orientation vector $\hat{\mathbf{e}}_{T_0}$ is given by

$$\hat{\mathbf{e}}_{T_0} = \frac{\mathbf{v}'_{fi} \cdot \mathbf{u}_i}{\left| \mathbf{v}'_{fi} \cdot \mathbf{u}_i \right|} \frac{\mathbf{v}'_{fi} \times \mathbf{u}_i}{\left\| \mathbf{v}'_{fi} \times \mathbf{u}_i \right\|} . \qquad (18)$$

The resultant torque is then expressed as $\mathbf{T}_p = T_p \hat{\mathbf{e}}_{T_0}$. For the torque coefficient, we use the expressions in Table 1 in this study. We do not include two-way coupling for the hydrodynamic torques i.e. there is a one-way coupling. Therefore, we only consider the influence of the flow on the particles. Similar to the lift force, we do not apply the Di Felice approximation to account for the effect of adjacent particles since it has not been derived for pitching torque.

3. Simulation parameters and void fraction calculation

Parameters for the CFD-DEM simulations are presented in Table 2. Particle material properties represent alumide particles that have been used in previous fluidisation experiments (Mahajan et al., 2017, 2018a). Reactor dimensions are equivalent to a laboratory scale apparatus. The incoming fluid velocity is set to $1.7U_{mf}$ to ensure operation in the bubbly regime. The minimum fluidisation velocity has been estimated from experiments (Mahajan et al., 2017, 2018a). The simulation time is equal to 18 s, which is more than sufficient for the system to attain a steady-state (Mahajan et al., 2018a). For the results presented in the next section, we assume that the system has reached steady-state after 5 s and we analyse the remaining 13 s of the simulation.

The dimensions of a grid cell used to solve the fluid flow with CFD are also presented in Table 2. In a CFD-DEM study on the fluidisation of monodisperse spherical particles, a grid cell size $c_{x,y,z}$ of least $1.6d_p$ has been proposed to accurately solve the fluid and solid phases (Peng et al., 2014), where d_p is the diameter of the volume equivalent sphere. Additionally, the grid cell size should not exceed $5d_p$, otherwise flow structures cannot be properly resolved. For spherocylinder particles, an additional criterion for an appropriate grid cell size is required such that a particle can be placed at the centre of a grid cell and freely rotated in all directions without intersecting any grid cell boundary. This prevents a particle from occupying 3 consecutive cells in any particular direction. A grid size of $2.83d_p$ can satisfy both criterions for the spherocylinders considered in this study. The size of the grid cell is also of relevance for the calculation of the drag force experienced by a particle (Eq. (11)). If the grid cell is too small, the local void fraction ϵ_f will be underestimated given that a cell may be almost entirely filled with a solid particle. Hence, the drag force as calculated with the Di Felice expression will be overestimated. In addition, a grid cell that is too small can lead to inaccurate solution of the continuity (Eq. (6)) and momentum conservation (Eq. (7)) expressions associated with the fluid. However, if the grid cell is too large, then local heterogeneities in the bulk and near boundaries cannot be resolved.

Finally, we present the approach used to calculate the fluid void fraction ϵ_f in each grid cell, which is required to solve the continuity equation (Eq. (6)), the momentum conservation equation (Eq. (7)), and for the calculation of the drag force on the particle. Calculation of the solid fraction contribution of a particle to any grid cell $\epsilon_s = 1 - \epsilon_f$ is subject to the following procedure. First, each particle is populated with a number of evenly-spaced satellite points n_{sp} throughout the particle volume where each point is assigned an equal weight or fraction of the particle volume. Second, the parent cell for a given particle is identified subject to the centre of mass position vector $\mathbf{r}_i$. Third, the particle volume is assigned to the parent cell and the adjacent cells subject to the location of the satellite points on the underlying grid. If the entire particle volume is located within the parent cell then no distribution of particle volume is necessary. If desired, the procedure can be optimised to allow for variation of n_{sp}.

4. Results

We now present simulation results of fluidised spherocylindrical particles subject to varying conditions of drag, lift, and torque. We will present results for seven different hydrodynamic force conditions, which are summarised in Table 3. We consider one case

Table 2
Relevant parameters for the CFD-DEM algorithm.

Parameter	Symbol	Value
CFD parameters		
Reactor base	L_x, L_y	0.15 m, 0.15 m
Reactor height	H_z	0.99 m
Number of grid cells	n_x^g, n_y^g, n_z^g	$10 \times 10 \times 66$
Grid cell dimensions	$c_x = c_y = c_z$	0.015 m
Min. fluidisation velocity	U_{mf}	1.7 m/s
Input fluid velocity	$V_f = 1.7U_{mf}$	2.89 m/s
Time step	t_{CFD}	1×10^{-4} s
Fluid density	ρ_f	1.2 kg/m³
Spherocylinder & DEM parameters		
Number of particles	N_p	30,000
Particle length	L	12 mm
Particle width	$2R$	3 mm
Particle aspect ratio	$L/2R$	4
Time step	t_{DEM}	1×10^{-5} s
Particle density	ρ_p	1395 kg/m³
Initial bed height	h_{init}	0.19 m
Coefficient of friction	μ	0.46
Cofficient of rolling friction	μ_r	0.46
Coefficient of restitution	e	0.43

Table 3
Hydrodynamic force cases explored in this study.

Case label	Drag force	Lift Force	Hydrodynamic torque
Drag N/A	only	Holzer-Sommerfeld (Eq. (9))	N/A
L_{Zast}	Holzer-Sommerfeld (Eq. (9))	Lift, Zastawny et al. (Table 1)	N/A
L_{Sanj}	Holzer-Sommerfeld (Eq. (9))	Lift, Sanjeevi et al. (Table 1)	N/A
T_{Zast}	Holzer-Sommerfeld (Eq. (9))	N/A	Torque, Zastawny et al. (Table 1)
T_{Sanj}	Holzer-Sommerfeld (Eq. (9))	N/A	Torque, Sanjeevi et al. (Table 1)
All_{Zast}	Holzer-Sommerfeld (Eq. (9))	Lift, Zastawny et al. (Table 1)	Torque, Zastawny et al. (Table 1)
All_{Sanj}	Holzer-Sommerfeld (Eq. (9))	Lift, Sanjeevi et al. (Table 1)	Torque, Sanjeevi et al. (Table 1)

where lift and torque are absent, denoted as "Drag only". In the "Drag only" case, the drag force includes the correlation of Holzer and Sommerfeld (Eq. (10)) with the Di Felice approximation (Eq. (11)) to account for the effects of surrounding particles on the drag. Thereafter all cases include this description of drag force. For the other cases, we consider varying lift and torque conditions using the correlation functions of Zastawny et al. (2012) and Sanjeevi et al. (2018) as specified in Table 1. We consider two cases of differing lift force (L_{Zast} and L_{Sanj}), two cases of differing torque force (T_{Zast} and T_{Sanj}) and two cases with both lift and torque (All_{Zast} and All_{Sanj}).

4.1. Particle dynamics

Fig. 4 shows five characteristic snapshots of a typical fluidisation cycle for two different hydrodynamic cases. In Fig. 4(a) we present a fluidisation cycle for a "Drag only" case while Fig. 4(b) shows the same cycle for a case where drag is supplemented with lift and torque (All_{Sanj}) from Sanjeevi et al. (2018). Both cycles start with an initial bed expansion (1) which terminates with a maximum bed expansion (3). The bed then releases and eventually returns to a configuration ready to undergo the fluidisation cycle once more. While it is difficult to decipher any differences between the cycles, there is some visual evidence to suggest that the particles are horizontally orientated to a greater extent upon the start of release for the case including lift and torque forces (Stage (4) in Fig. 4(b)). We will explore this response quantitatively in the proceeding sections.

Fig. 5 shows the variation of the temporally-averaged number of particles or particle occupancy $\langle n_p \rangle$ with reactor height in the z-direction for a number of hydrodynamic force cases. We note that variation of $\langle n_p \rangle$ with z is effectively invariant to changes in the hydrodynamic force conditions. The dip in $\langle n_p \rangle$ for $z < 0.06$ m is due to the proximity of this domain to the fluidisation velocity, which leads to a slightly lower density of particles in this layer by pushing the particles into the layers above. The upper domain of the reactor $z > 0.45$ m is quite dilute with $\langle n_p \rangle \leqslant 2$.

4.2. Particle velocity along z-axis

Fig. 6(a) shows a snapshot of the fluidised bed with rigid boundaries located along the x-axis and y-axis. We sample the particle velocity along the gravity direction (z-axis) denoted as v_z at three positions in the reactor, as shown in Fig. 6(b), where $z = 0.0675$ m is closest to the bottom of the reactor or the flow inlet, and $z = 0.3075$ m is furthest for the flow inlet and a region with dilute particle conditions. These positions are approximately midway along the y-axis (0.06 m $\leqslant y \leqslant 0.075$ m). We have also highlighted these positions in Fig. 5. Evidently from the snapshot in Fig. 6, just as for Fig. 5, we find that particle occupancy is higher close to the bottom of the reactor while at the highest position considered here particle flow is more dilute.

We now consider the effect of hydrodynamic force conditions on the particle velocity parallel to the direction of gravity. We

Fig. 4. Visualisation of a typical fluidisation cycle lasting approximately 1.2 s. (a) Drag only. (b) All_{Sanj}. Five characteristic snapshots are shown and labelled as follows: (1) Start of bed expansion; (2) Mid-way of bed expansion; (3) Maximum bed expansion; (4) Start of release; (5) End of release. These system snapshots were visualised using OVITO (Stukowski, 2010)).
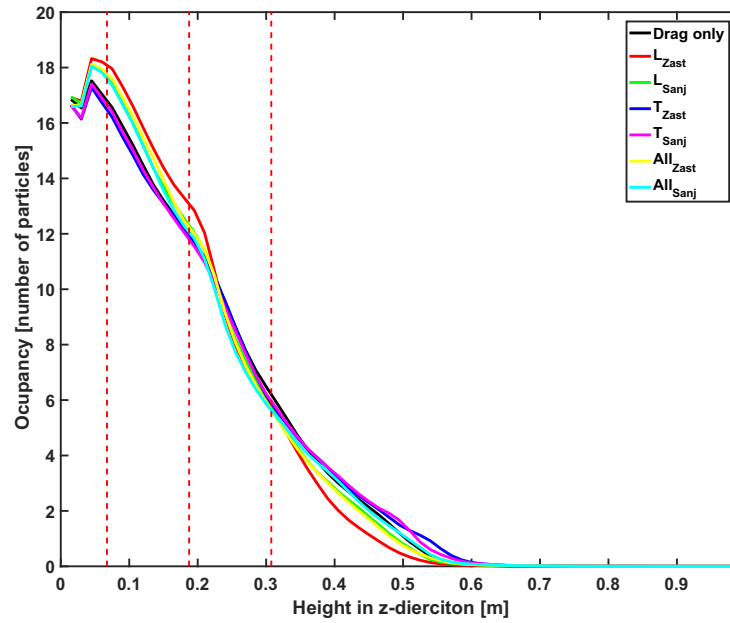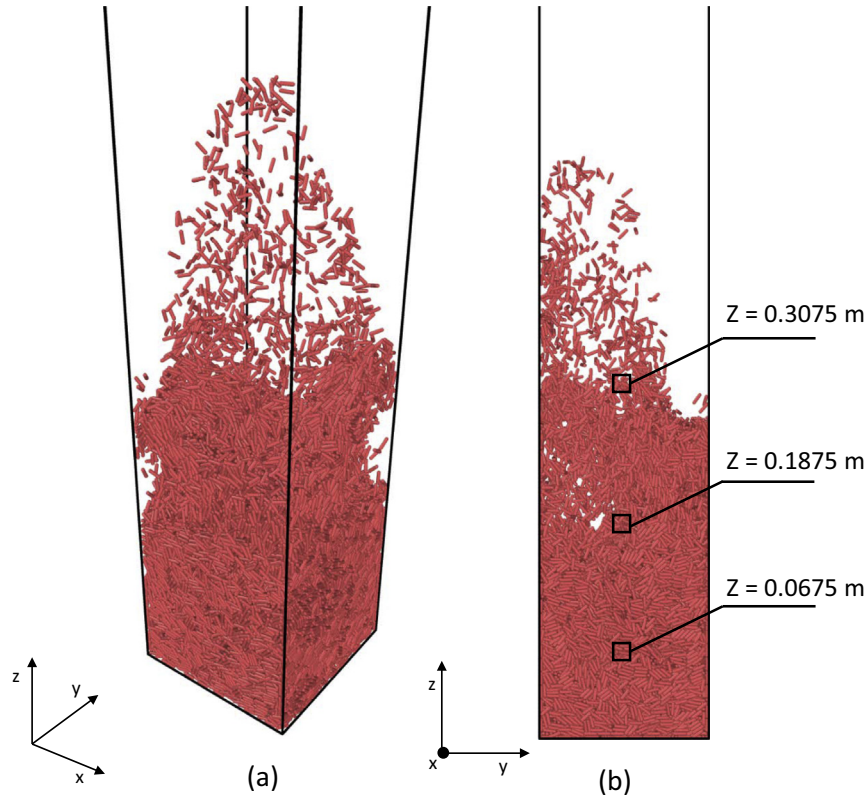
Fig. 5. Variation in the particle occupancy $\langle n_p \rangle$ with reactor height. The red dashed lines indicate the positions along the z-axis used for the calculation of v_z profiles in Section 4.2. (For interpretation of the references to colour in this figure legend, the reader is referred to the web version of this article.)

Fig. 6. (a) Snapshot of the fluidised bed reactor with fluid velocity $1.7U_{mf}$ where the hydrodynamic force case is "Drag only". (b) Analysis positions in the bed reactor along the z-direction. These system snapshots were visualised using OVITO (Stukowski, 2010)).

constructed temporally averaged profiles along the x-axis in the range $0.0\,\text{m} \leqslant x \leqslant 0.15\,\text{m}$ and for fixed y-axis and z-axis positions as illustrated in Fig. 6. The temporally-averaged particle velocity along the z-direction v_z at a given grid cell in the fluidised bed reactor over a specific time interval is calculated using the expression

$$v_z = \frac{\sum_{t=t_0}^{t_{\text{end}}} \sum_{p=1}^{N_{\text{cell}}(t)} v_z(p,t)}{\sum_{t=t_0}^{t_{\text{end}}} N_{\text{cell}}(t)} \tag{19}$$

where t_0 is the start time, t_{end} is the end time, $N_{\text{cell}}(t)$ is the number of particles in the grid cell at time t, p is the particle label, and

$v_z(p, t)$ is the velocity of particle p in the grid cell at time t. We note that the average velocity v_z is not the same as the average mass flux, because there may be strong correlations between the local solids volume fraction and the instantaneous velocity of a particle. This has recently been shown experimentally for spherocylindrical particles in a pseudo-2D fluidised bed (Mahajan et al., 2018a)

Fig. 7 shows that the inclusion of lift has a noticeable effect on v_z throughout the reactor while torque has a negligible effect on v_z. For example, at $z = 0.0675$ m, inclusion of the correlation for lift (L_{Zast}) leads to a large increase in v_z approximately halfway along the x-axis in comparison to the case where particles are only subject to drag. We observe an analogous behaviour upon consideration of the Sanjeevi lift correlation (L_{Sanj}) although the increase in v_z is lower than with the inclusion of the Zastawny lift correlation (L_{Zast}). Similar trends are also recorded at other heights in the reactor although at $z = 0.3075$ m the differences between the trends

are not as pronounced as at $z = 0.0675$ m. This may be attributed in part to the lower particle density, and hence increase in void fraction, at higher positions in the bed. A typical representation of this decrease in particle density is evident in the snapshot of particle fluidisation shown in Fig. 6. On the other hand, inclusion of either the Zastawny or Sanjeevi torque correlation has little or no effect on the velocity profiles. For cases with all hydrodynamic forces, there is no significant change in v_z in comparison to cases with just drag and lift force. This demonstrates that torque does not appreciably affect v_z, even in combination with lift force.

The changes in the v_z profiles observed here with the inclusion of lift force are similar to those noted in our previous study of particle dynamics in a small reactor (Mema et al., 2017). Here v_z increases halfway along the x-axis upon inclusion of lift force while in the study on a small reactor, we also find a similar increase in v_z along the x-axis. However, in the previous study, we also applied
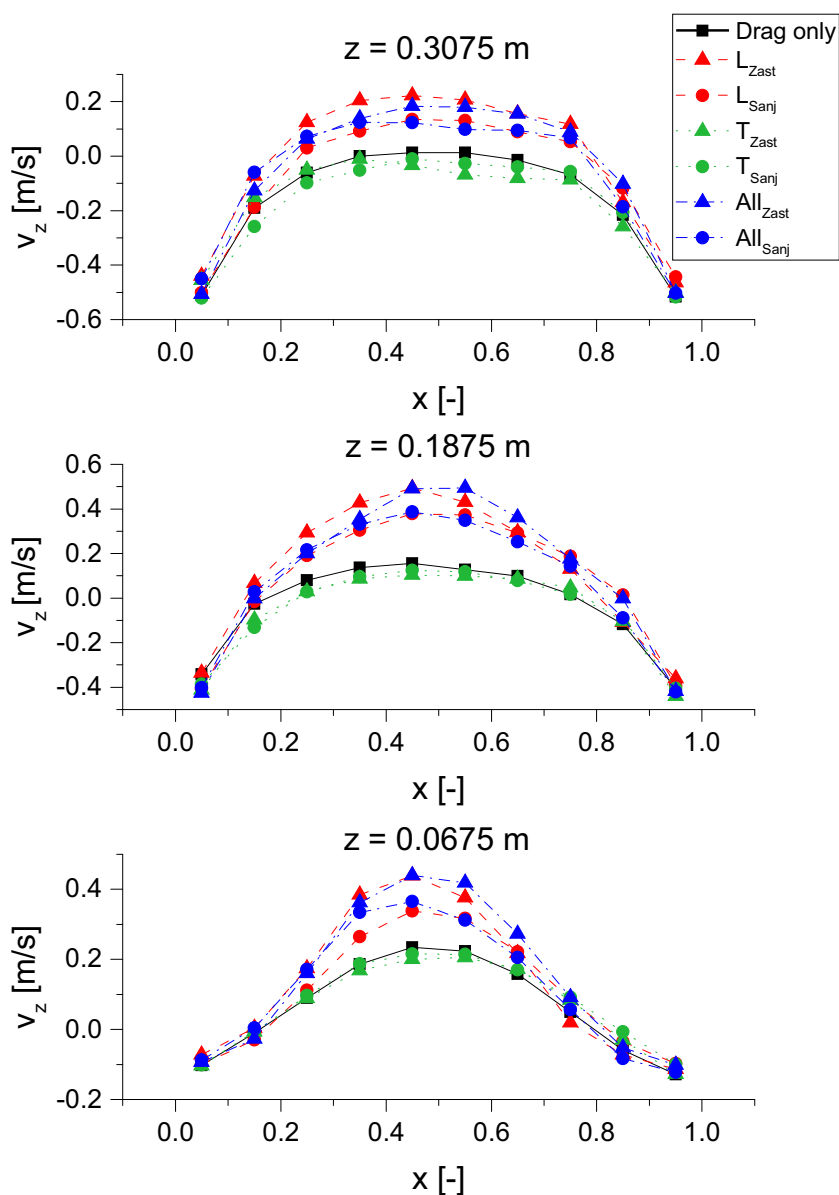
Fig. 7. Comparison of the temporally-averaged v_z along the x-axis for the positions defined in Fig. 6(b) in a fluidised bed reactor for different hydrodynamic conditions: Drag only, lift force described by Zastawny (L_{Zast}), lift force described by Sanjeevi (L_{Sanj}), HD Torque described by Zastawny (T_{Zast}) and by Sanjeevi (T_{Sanj}). In these plots, x is the position normalised by the length of reactor along the x-axis (0.15 m). Cases with lift force are presented as red dashed lines (‒ ‒ ‒ ‒), cases with torque with the green dotted line (•••••), and cases with all forces included with the blue dash-dot lines. (‒ • ‒ • ‒). The filled triangles represents cases of Zastawny et al. (2012) and the filled circles are cases using the correlations of Sanjeevi et al. (2018).

the Di Felice expression to the lift force to further explore the effect of varying lift conditions. The results showed that with the Di Felice expression the lift force effects become even stronger.

4.3. Particle orientation

We now consider variations in particle orientation parallel to the direction of flow. Fig. 8 shows the variation of the temporally-averaged fraction of particles f_p with a certain orientation relative to the z-axis for different hydrodynamic force conditions. If $u_z = \pm 1$ the particle is fully aligned with the flow while at $u_z = 0$ the particle is perpendicular to the flow. All trends are calculated in steady-state using the expression

$$f_p(u_z) = \frac{1}{(t_{end} - t_0)h_{u_z}} \sum_{t=t_0}^{t_{end}} \frac{n_p(u_z, t)}{N_p} \qquad (20)$$

where $n_p(u_z)$ is the number of particles with an orientation u_z at time t, N_p is the number of particles in the reactor, and the bin width $h_{u_z} = 0.05$. Fig. 8 shows that for the case of drag only and the cases with drag and lift only the majority of particles tend to align with the direction of the fluid flow. From the figure it can also be concluded that the introduction of lift has little or no effect on the preferred orientation of particles. Upon inclusion of the hydrodynamic torque expressions there is a discernible change in the trend with the majority of particles tending to orient perpendicular to the flow. This is demonstrated for both Zastawny's and Sanjeevi's torque correlation functions. Inclusion of lift force along with drag and torque leads to little or no change in the preferred orientation of particles as observed for cases with all forces described by Zastawny and Sanjeevi correlations (All$_{Zast}$ and All$_{Sanj}$).

While Fig. 8 demonstrates the average orientation of particles with respect to the z-axis, it does not provide information with regards to preferred particle orientations in specific domains of the reactor. To resolve the preferred particle orientation we calculate the particle orientation tensor $\mathbf{S}_i$ using the expression

$$\mathbf{S}_i = \begin{bmatrix} \langle u_x^2 \rangle & \langle u_x u_y \rangle & \langle u_x u_z \rangle \\ \langle u_y u_x \rangle & \langle u_y^2 \rangle & \langle u_y u_z \rangle \\ \langle u_z u_x \rangle & \langle u_z u_y \rangle & \langle u_z^2 \rangle \end{bmatrix}. \qquad (21)$$

The diagonal components of this tensor can be used to determine the preferred alignment in the reactor. If the difference between

the diagonal components is less than 0.1 i.e. $\left| \langle u_x^2 \rangle - \langle u_y^2 \rangle \right| < 0.1$, $\left| \langle u_x^2 \rangle - \langle u_z^2 \rangle \right| < 0.1$ and $\left| \langle u_y^2 \rangle - \langle u_z^2 \rangle \right| < 0.1$, the particle is considered to be randomly oriented. On the other hand, if one component is considerably larger than the other two components, we conclude that the particle is preferably aligned with the corresponding axis.

Figs. 9–11 show the preferred particle alignment in steady-state in the grid cells for different lift and torque force conditions respectively. We study the particle alignment in the grid cells on the x-z plane and for a cross section along the y-axis (0.06 m $\leqslant y \leqslant$ 0.075 m). From Table 2 the number of grid cells along the x-axis and z-axis are $n_x^g = L_x/c_x = 10$ and $n_z^g = H_z/c_z = 66$ respectively. We have applied a colour scheme to differentiate cells with particular particle orientations with blue cells indicating a preferred alignment with the x-axis, green cells indicating a preferred alignment with the y-axis, and red cells indicating a preferred alignment with the z-axis. Cyan cells represent domains where there is no preferred orientation such that particles are randomly orientated.

From Fig. 9 we observe that inclusion of the lift force with drag does not lead to large changes in the preferred orientation of particles near the base of the reactor i.e. up to $z = 15$. However, we note that the particle orientations tend to become more random in the central domains of the reactor. With increasing height, differences between the preferred orientations are negligible due to the low density of particles in these domains of the reactors. With the inclusion of torque (Fig. 10), we find a noticeable effect on particle orientation as we have already observed in Fig. 8. Rather than being predominantly aligned with the z-axis, the particles are now aligned either randomly or perpendicular to the z-axis i.e. aligned with the x-axis and y-axis. We also highlight a change in the alignment of particles next the boundaries in comparison to the inclusion of lift (Fig. 9). In the cases with lift, particles near the walls tends to be aligned with the z-axis, while for cases with torque the particles tend to align with the y-axis. In addition, hydrodynamic torque has a strong influence on particle orientation in the diluted domain of the reactor, in particular in the range $30 < z < 50$ where particles have a strong preferred horizontal orientation. This is indicative of the rotational effects of torque to align particles perpendicular to the fluid flow. In the lowest section of the reactor ($z < 20$), particles retain a preferred vertical orientation even with the inclusion of hydrodynamic torque. Fig. 11 shows the effect of combined lift and torque conditions on the spatial
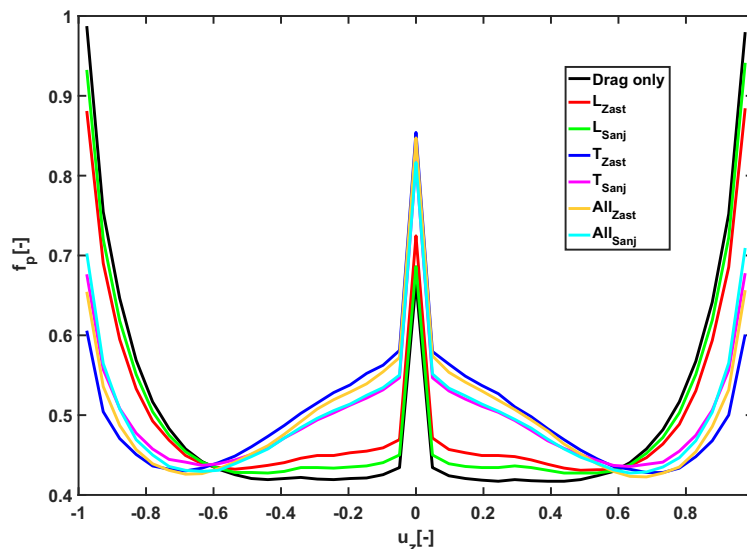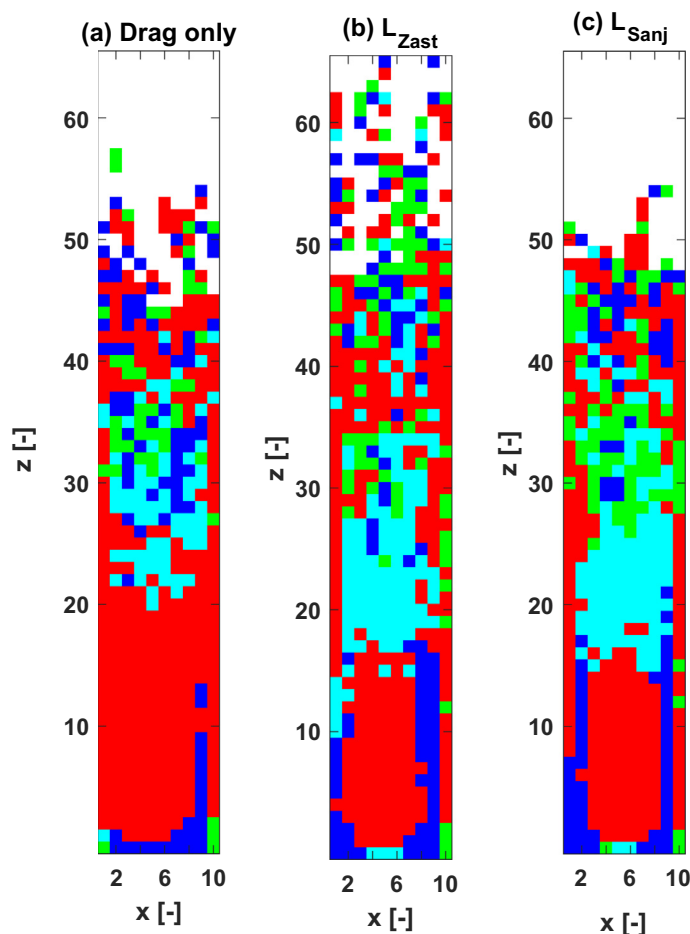

Fig. 8. Preferred particle orientation. Variation of $f_p(u_z)$ for differing hydrodynamic force conditions.

Fig. 9. Preferred orientation of particles in the grid cells of the reactor for different cases of hydrodynamic force; with drag only and cases with lift force. (a) Drag only. (b) L_{Zast}. (c) L_{Sanj}. Here the colour scheme is: blue squares (■) are x-aligned, green squares (■) are y-aligned, red squares (■) are z-aligned, and cyan squares (■) are randomly orientated. White space represents empty cells. The dimensions of the reactors on the x-z plane are $L_x \times H_z = 0.15$ m $\times$ 0.99 m. In this plot, the dimensions are normalised by the grid cell size thus leading to $n_x^g = L_x/c_x = 10$ and $n_z^g = H_z/c_z = 66$.

distribution of preferred orientation. Similar to Fig. 8, we do not see any large difference in particle orientations upon inclusion of lift with drag and hydrodynamic torque. The majority of particles tend to orient horizontally with particles in the lower section of the reactor having a preferred vertical orientation. Comparing Figs. 10 and 11 we highlight a slight difference in particle orientation in the central section of reactor between i.e. $15 < z < 30$, where particles have a preferred horizontal orientation. We also find a slight increase of particles vertically aligning adjacent to the walls, which is similar to the effect noted for cases with just drag and lift.

4.4. Angular momentum

Figs. 12–14 show the temporally-averaged magnitude of the angular momentum at grid cells on the x-z plane averaged along the y-axis for different hydrodynamic force conditions. We notice that particles have the largest angular momentum in the freeboard or upper region of the bed where particle flow is quite dilute with the average particle occupancy $\langle n_p \rangle < 2$ (Fig. 5). Comparing Figs. 12 and 13, we note that the inclusion of lift only leads to a considerable increase in angular momentum, while the inclusion of hydrodynamic torque only has almost no effect on particle rotation. In addition, use of the Zastawny et al. lift correlation leads to a much larger change in angular momentum in comparison to the results with the Sanjeevi et al. lift correlation. The greater influence of lift force on particle rotation can be attributed to the generation of lar-

ger torques by particle-particle and particle-wall interactions in contrast to hydrodynamic forces. As presented in Section 4.2, the inclusion of lift force leads to an increases in v_z, and consequently, more vigorous particle interactions, which results in larger variations in angular momentum. Including hydrodynamic torque has considerably less effect on particle rotation and it actually stabilises the particles, thus inhibiting free rotation, which is caused by the hydrodynamic torque always acting in the direction opposite to particle rotation. When all forces are included (Fig. 14), there is little difference with the case of drag and lift only (Fig. 12), which indicates that lift force has the dominant effect on particle rotation. From the comparison of Figs. 12 and 14 we conclude that the inclusion of hydrodynamic torque has a stabilising effect on particle rotation, hence lowering the total angular momentum.

5. Discussion and conclusion

We have investigated via numerical simulations the effect of differing hydrodynamic force conditions on spherocylindrical particles (aspect ratio = 4) in dense gas-fluidised beds. To account for the coupling between the solid particle phase and fluid phase, we have employed the CFD-DEM algorithm where the CFD component solves the fluid motion and DEM solves the particle-particle interactions. In this study, we have considered several hydrodynamic force cases where particles are subject to varying lift and torque
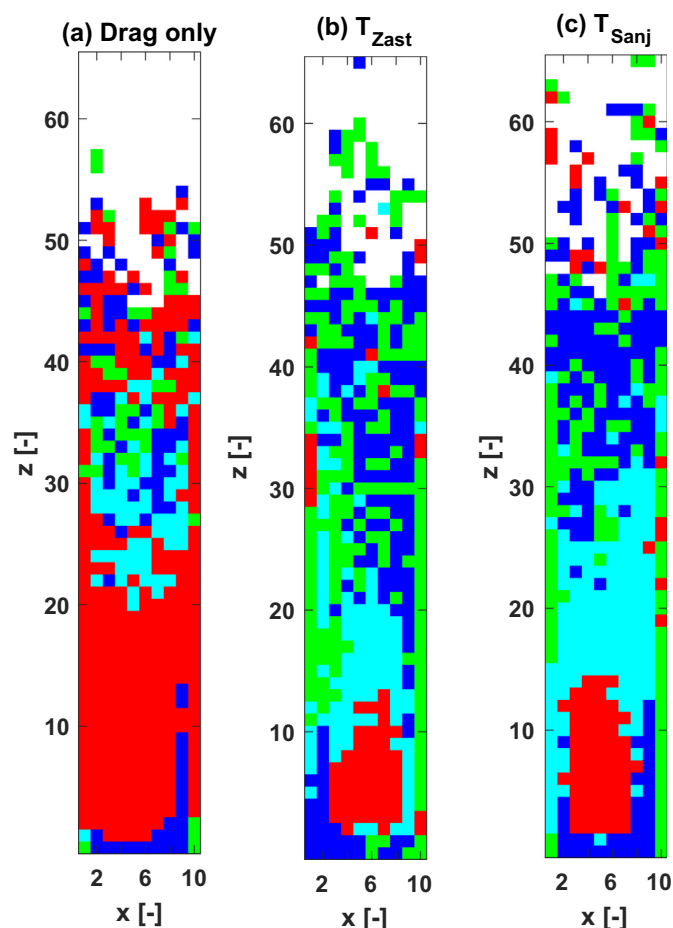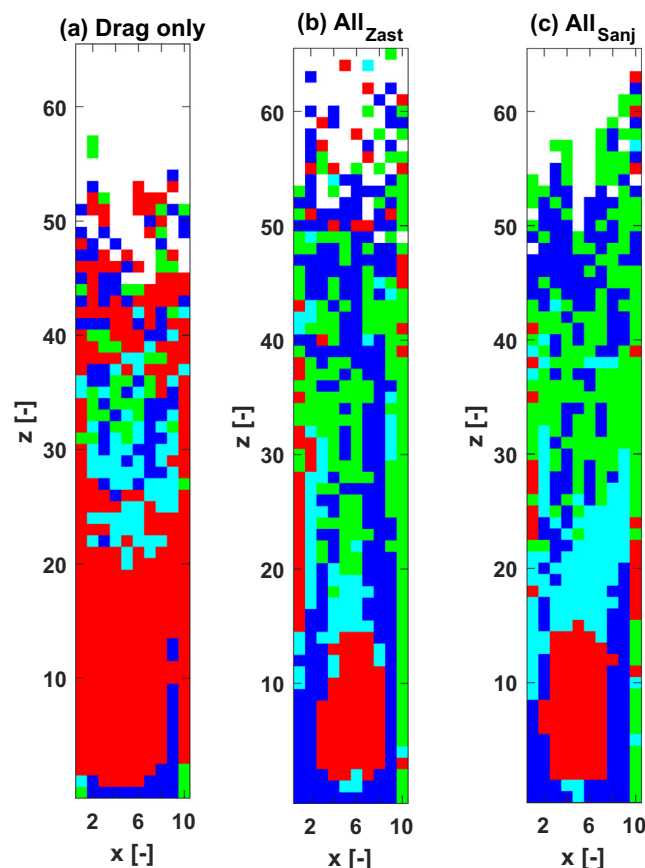
Fig. 10. Preferred orientation of particles in the grid cells of the reactor for different cases of hydrodynamic force; with drag only and cases with hydrodynamic torque. (a) Drag only. (b) T_{Zast}. (c) T_{Sanj}. Details of the colour scheme are provided in the caption of Fig. 9.

Fig. 11. Preferred orientation of particles in the grid cells of the reactor for different cases of hydrodynamic force; with drag only and cases with all forces included. (a) Drag only. (b) All_{Zast}. (c) All_{Sanj}. Details of the colour scheme are provided in the caption of Fig. 9.

closures (Table 3). First, we have used lift and torque expressions from Zastawny et al. (2012) that were derived for ellipsoids and disk-like particles. From in-house direct numerical simulations (DNS), fitting coefficients suitable for spherocylindrical particles in this study have been calculated for the expressions of Zastawny et al. (2012). Second, we have employed lift and torque expressions specifically for the spherocylindrical particles explored in this study from the recent DNS simulations of Sanjeevi et al. (2018). While we account for multiparticle effects in the calculation of the drag force by using the Di Felice approximation (Felice, 1994), the correlation functions considered here for the estimation of the lift and torque have been derived for isolated single spherocylinder particles and thus are applied here as an approximation of lift and torque conditions in a dense fluidised bed.

While we have explored a number of hydrodynamic force cases, a key observation from the results is the relevance of hydrodynamic torque on particle dynamics, in particular on particle orientation. In Section 4.3, we examined the effect of differing hydrodynamic force conditions on particle orientation with respect to the fluid flow or z-axis over the entire reactor and in specific domains of the reactor. First, Fig. 8 revealed that inclusion of torque leads to a considerable change in particle orientations, with particles less likely to be orientated parallel to the flow and more likely to be orientated perpendicular to the flow. We confirmed this observation by studying preferred particle orientations for dif-

fering lift and torque conditions. Second, although the addition of lift only has a slight effect on particle orientation (Fig. 9), marked by an increase in random orientation of particles in the middle section of the reactor, the inclusion of torque leads to considerable changes in the particle orientations throughout the reactor (Fig. 10). We note that only particles near the flow inlet of the reactor show alignment with the direction of fluid flow for both lift force cases. This is more than likely due to the collation of contacting particles into groups that move as a single solid unit with the direction of fluid flow. Beyond this region the particles become randomly orientated after which the particles tend to align perpendicular to the direction of flow (Fig. 10). This conforms with the visualisations presented in Fig. 4 where during the start of release particles appear to be orientated perpendicular to the z-axis. Additionally, the inclusion of torque leads to a large decrease in particle alignment with the z-axis for particles adjacent to the boundaries. Without torque, the particles can rotate more freely, however with torque, the degree of particle rotation decreases such that particles tend to orient perpendicular to the fluid flow. We do not find an appreciable difference in particle angular momentum with or without hydrodynamic torque or lift (see Figs. 12–14). This suggests that changes in particle angular momentum may be dominated by interparticle interactions.

We also examined the effect of varying hydrodynamic forces on particle velocity along the z-axis (v_z) at specific locations in the reactor (Fig. 7). For cases with just torque we find that there is little or no difference in the velocity profile in comparison to the case with drag forces only. However, inclusion of lift leads to a drastic
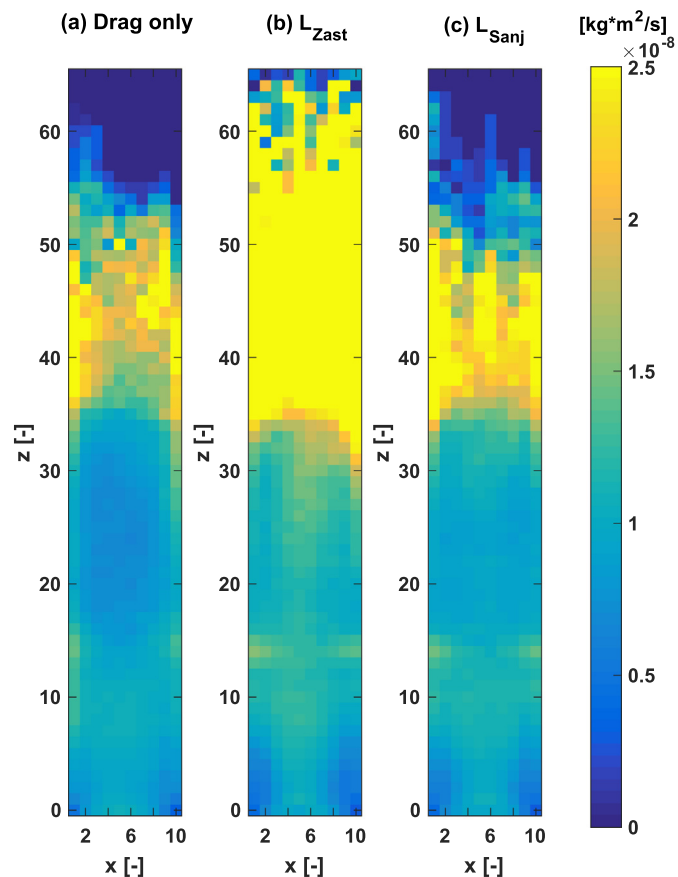
Fig. 12. Angular momentum in *x-z* plane, temporally-averaged and averaged through *y*-direction for cases with (a) Drag only and (b, c) Drag and lift.

Fig. 13. Angular momentum in *x-z* plane, temporally-averaged and averaged through *y*-direction for cases with (a) Drag only and (b, c) Drag and torque.

change in the profile when compared with a case of just hydrodynamic torque, in particular midway along the x-axis. These results indicate that lift has a greater influence than hydrodynamic torque on particle velocity. However, while lift affects particle velocity, torque has a marked affect on particle orientation (Fig. 8). In combination, lift and torque conditions are of paramount importance for the interactions experienced by particles, and hence on the resulting flow conditions. We must also emphasise that both the lift and torque are calculated without consideration of multiparticle effects. Our previous study suggests that a multiparticle expression for lift force can have an even stronger effect on v_z profiles than using the single particle expression (Mema et al., 2017). To comprehensively establish the precise effect of lift and torque in a multiparticle setting requires new multiparticle expressions for the calculation of the lift and torque that could be derived from DNS simulations similar to those used to define the isolated lift and torque correlations (Sanjeevi et al., 2018).

While single-particle lift and torque correlations do not account for multiparticle effects and may lead to an overestimation of lift and torque in the dense or lower bulk domains of the reactor, particle dynamics in the upper domains of the reactor are argued to have greater accuracy. As shown in Fig. 5, temporally-averaged particle occupancy $\langle n_p \rangle$ in the upper domains of the reactor are significantly lower than in dense domains. For example, at $z = 0.0675$ m, which lies in the dense region of the reactor, $\langle n_p \rangle \approx 17$. However, at $z = 0.3075$ m, which lies in the dilute domain of the reactor, $\langle n_p \rangle \approx 5$. Hence, in the upper regions of the bed, on average, particles will be subject to lower multiparticle effects and thus lower deviations from the idealised single particle
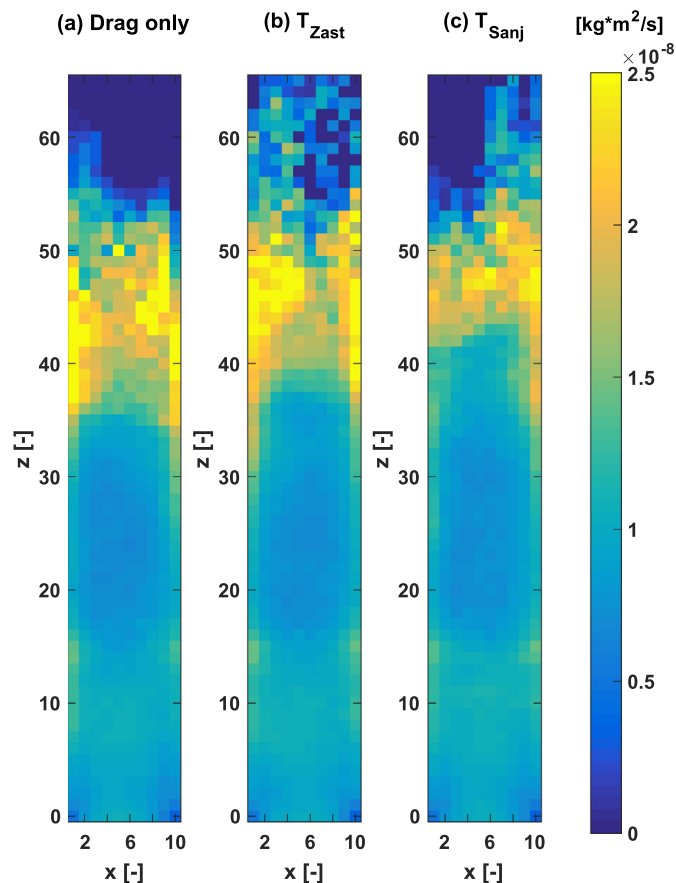
case. Thus, we surmise that the lift and torque conditions experienced by particles, and hence the ensuing dynamics in the upper regions of the bed can be suitably described using single-particle lift and torque correlations. Further studies on varying lift and torque conditions are necessary to corroborate this effect.

Domains near the base of the reactor are typified by long-lasting particle contacts and groups of interlocked or jammed particles. These groups will tend to move as single units and thus experience hydrodynamic conditions dictated by local multiparticle effects. Intuitively one would expect that the lift and torque on an individual particle in a group would be suppressed. The lift and torque correlations used in this study do not account for such complex multiparticle effects. Imperatively, we point out that this study is a preliminary investigation on the importance of lift and torque on fluidised spherocylinders. Once accurate and appropriate multiparticle lift and torque correlations become available, we will perform further simulations to explore particle dynamics and fully assess the limitations of single-particle lift and torque correlations for spherocylinders.

We have also not considered rotational torque, which develops due to the relative rotation of a particle with respect to the fluid. An expression for rotational torque has been defined in a previous study on ellipsoids and disk-like particles (Zastawny et al., 2012). However, the coefficients are not applicable to the spherocylinders studied here. In addition, we deemed that rotational torque was not relevant for particle dynamics. Nonetheless, an accurate expression for spherocylindrical rotational torque could be calculated with DNS simulations for future CFD-DEM investigations.
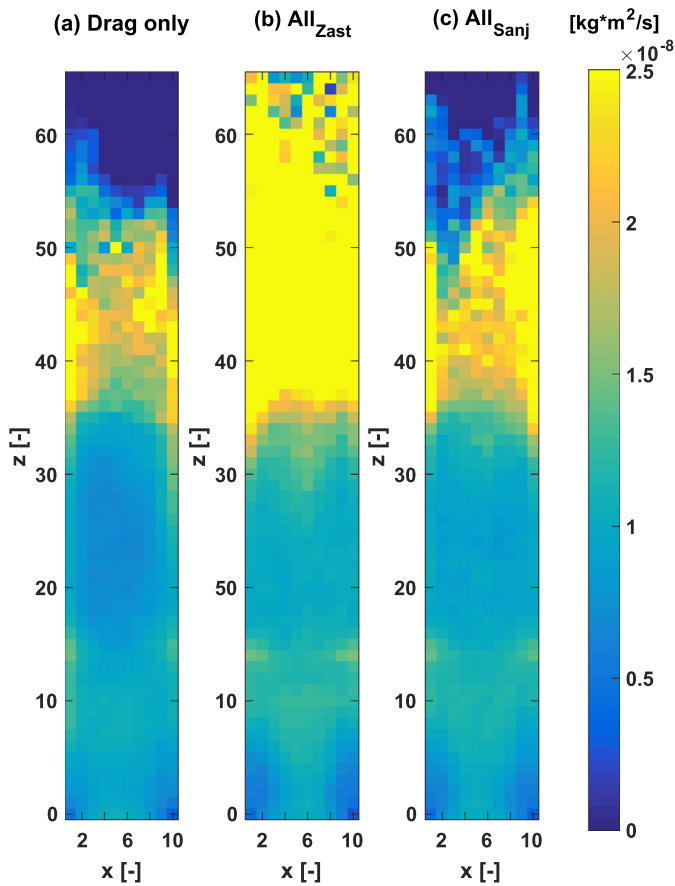
Fig. 14. Angular momentum in *x-z* plane, temporally-averaged and averaged through *y*-direction for cases with (a) Drag only and (b, c) all hydrodynamic forces included.

In the case of the drag closure, with multiple-particle correlation expressions for spherocylinder particles unavailable, we account for the effect of neighbouring particles by adapting the expression of Di Felice (Eqs. (11) and (12)). However, the Di Felice approximation has been derived for spherical particles (Felice, 1994) and is used here to approximate the neighbouring or swarm effect on the drag forces experienced by spherocylindrical particles. Previous studies on spherocylinder-like particles have also employed the Di Felice expression to account for multiple-particle effects (Hilton et al., 2010; Vollmari et al., 2016; Gan et al., 2016; Ma and Zhao, 2018a; Ma and Zhao, 2018b). While the Di Felice expression accounts for variations in the particle Reynolds number, it does not take into consideration the orientation of the particle of interest or the orientation of the neighbouring particles, given that it has been defined for perfect spheres. As a result, the expression may coarse grain key geometrical aspects of particle arrangements near a particle of interest and hence provide only a rough estimate of the true drag force. Compared to the spherical case, the change in drag force experienced by a spherocylinder due to the proximity of other spherocylinder particles may depend on the configuration of the neighbouring particles.

Experiments with pseudo-2D fluidised beds can be used for accurate particle image velocimetry (PIV) and particle tracking velocimetry (PTV) studies (Mahajan et al., 2018a). Unfortunately such experiments do not provide information in relation to particle dynamics in the bulk of a fluidised bed i.e. distant from the boundaries of the system.

To gain better insight into the fluidisation response in laboratory scale 3D fluidised beds, in the future, we plan to perform

Magnetic Particle Tracking (MPT) experiments (Buist et al., 2014; Buist et al., 2017; Khler et al., 2017) where the magnetic field associated with a single magnetic tracer particle is measured using a magnetic sensor array. This approach has previously been used to track both spheres and rods in a cylindrical fluidised bed (Buist et al., 2017). Data from future MPT experiments will be compared with current numerical results and also used to motivate further CFD-DEM investigations.

Appendix: Lift and torque coefficients

In this study, we explored the effect of varying lift and torque expressions on the dynamics of fluidised non-spherical particles. These expressions were derived for a single rest particle in a particle flow at varying angles of incidence and Reynolds number using direct numerical simulations (DNS). Here the angle of incidence is defined as the angle between the direction of the fluid flow and the principal or longest axis of the non-spherical particle. For instance, Sanjeevi et al. (2018) modelled the flow via the D3Q19 multi-relaxation time (MRT) lattice Boltzmann method (LBM).

The lift and torque correlation functions from the DNS investigations of Sanjeevi et al. (2018) and Zastawny et al. (2012) used in this study are presented in Table 1. Each function is comprised of a number of coefficients that have been estimated by fitting the correlation functions in Table 1 to data from direct numerical simulations. In the study of Zastawny et al. (2012), these coefficients were calculated for ellipsoids, disc-shaped particles and fibres with an aspect ratio of 5. However, these parameters are not applicable for the spherocylinders used in this study, which have an aspect ratio of 4. Therefore, we use coefficients for L_{Zast} and T_{Zast} that have been fitted using in-house DNS simulations. For further information on the DNS simulations we refer the reader to references Sanjeevi and Padding (2017) and Sanjeevi et al. (2018). The coefficients for the Zastawny lift and torque functions are presented in Table A.1 while the coefficients for the Sanjeevi lift and torque functions are given in Table A.2.

Table A.1
Coefficients for the lift and torque correlations of Zastawny et al. (2012) fitted for spherocylinder particles with aspect ratio of 4 using in-house DNS simulations.

Lift		Torque	
Coefficient	Value	Coefficient	Value
b_1^Z	1.884	c_1^Z	−2.283
b_2^Z	0.1324	c_2^Z	−0.01145
b_3^Z	0.001668	c_3^Z	4.09
b_4^Z	−0.8159	c_4^Z	−0.01395
b_5^Z	0.8562	c_5^Z	0.3406
b_6^Z	0.003624	c_6^Z	0.3609
b_7^Z	0.6598	c_7^Z	0.1355
b_8^Z	−0.2621	c_8^Z	0.2356
b_9^Z	0.8021	c_9^Z	0.3612
b_{10}^Z	0.04384	c_{10}^Z	0.1358

Table A.2

Coefficients for the lift and torque correlations of Sanjeevi et al. (2018) for a spherocylinder particle with aspect ratio of 4.

Lift		Torque	
Coefficient	Value	Coefficient	Value
b_1^S	6.718	c_1^S	5.079
b_2^S	0.069	c_2^S	0.342
b_3^S	−0.378	c_3^S	0.197
b_4^S	2.666	c_4^S	−0.161
b_5^S	0.314	c_5^S	0
b_6^S	0.046	c_6^S	0
b_7^S	0.345	c_7^S	0
b_8^S	3.50×10^{-5}	c_8^S	0
b_9^S	1.194		

References

Aharonov, E., Sparks, D., 1999. Phys. Rev. E 60, 6890.

Aharonov, E., Sparks, D., 2002. Phys. Rev. E 65, 051302.

Alauddin, Z.A.B.Z., Lahijani, P., Mohammadi, M., Mohamed, A.R., 2010. Renew. Sustain. Energy Rev. 14, 2852.

Azéma, E., Radjaï, F., 2012. Phys. Rev. E 85, 031303.

Bridgwater, A., 2003. Chem. Eng. J. 91, 87.

Bridgwater, T., 2006. J. Sci. Food Agric. 86, 1755.

Buist, K.A., van der Gaag, A.C., Deen, N.G., Kuipers, J.A.M., 2014. AIChE J. 60, 3133.

Buist, K.A., Jayaprakash, P., Kuipers, J., Deen, N.G., Padding, J.T., 2017. AIChE J. 63, 5335.

Cai, W., Liu, R., He, Y., Chai, M., Cai, J., 2018. Fuel Process. Technol. 171, 308.

Chen, G., Liu, J., Yao, J., Qi, Y., Yan, B., 2017. Energy Convers. Manage. 138, 556.

Cundall, P., Strack, O., 1979. Geotechnique 21, 47.

Deen, N., Annaland, M.V.S., der Hoef, M.V., Kuipers, J., 2007. Chem. Eng. Sci. 62, 28.

Felice, R.D., 1994. Int. J. Multiph. Flow 20, 153.

Fitzgerald, B.W., Clancy, I., Corcoran, D., 2014. Physica A 410, 582.

Gan, J., Zhou, Z., Yu, A., 2016. Chem. Eng. Sci. 144, 201.

Ganser, G.H., 1993. Powder Technol. 77, 143.

Gil, M., Teruel, E., Arauzo, I., 2014. Fuel 116, 328.

Grace, J.R., Avidan, A., Knowlton, T., 1997. Circulating Fluidized Beds. Hoerner Fluid Dynamics.

Haider, A., Levenspiel, O., 1989. Powder Technol. 58, 63.

Haustein, M., Gladkyy, A., Schwarze, R., 2017. SoftwareX6 118.

Hilton, J., Mason, L., Cleary, P., 2010. Chem. Eng. Sci. 65, 1584.

Hölzer, A., Sommerfeld, M., 2008. Powder Technol. 184, 361.

Hölzer, A., Sommerfeld, M., 2009. Comput. Fluids 38, 572.

Khler, A., Rasch, A., Pallarés, D., Johnsson, F., 2017. Powder Technol. 316, 492.

Kloss, C., Goniva, C., Hager, A., Amberger, S., Pirker, S., 2012. Prog. Comput. Fluid Dynam. 12, 140.

Kruggel-Emden, H., Vollmari, K., 2016. Particuology 29, 1.

Kumar, R., Sarkar, A., Katterhagen, W., Hancock, B., Curtis, J., Wassgren, C., 2018. AIChE J. 64, 1986–2001.

Loth, E., 2008. Powder Technol. 182, 342.

Ma, H., Zhao, Y., 2018a. Powder Technol.

Ma, H., Zhao, Y., 2018b. Adv. Powder Technol.

Mahajan, Vinay V., Nijssen, Tim M.J., Fitzgerald, Barry W., Hofman, Jeroen, Kuipers, Hans, Padding, Johan T., 2017. EPJ Web Conf. 140, 06019.

Mahajan, V.V., Nijssen, T.M., Buist, K.A., Kuipers, J.A.M., Padding, J.T., 2018a. AIChE J. 64, 1573–1590.

Mahajan, V.V., Nijssen, T.M., Kuipers, J.A.M., Padding, J.T., 2018b. Chem. Eng. Sciencel 192, 1105–1123.

Mandø, M., Rosendahl, L., 2010. Powder Technol. 202, 1.

Marschall, T., Teitel, S., 2018. Phys. Rev. E 97, 012905.

Mattisson, T., Keller, M., Linderholm, C., Moldenhauer, P., Rydén, M., Leion, H., Lyngfelt, A., 2018. Fuel Process. Technol. 172, 1.

McKendry, P., 2002. Bioresour. Technol. 83, 55.

Mema, I., Mahajan, V.V., Fitzgerald, B.W., Kuipers, H., Padding, J.T., 2017. In: Proceedings of 12th International Conference on CFD in Oil and Gas, Metallurgical and Process Industries.

Nikoo, M.B., Mahinpey, N., 2008. Biomass Bioenergy 32, 1245.

Ouchene, R., Khalij, M., TaniÈre, A., Arcen, B., 2015. Comput. Fluids 113, 53.

Ouchene, R., Khalij, M., Arcen, B., TaniÈre, A., 2016. Powder Technol. 303, 33.

Peng, Z., Doroodchi, E., Luo, C., Moghtaderi, B., 2014. AIChE J. 60, 2000.

Pournin, L., Weber, M., Tsukahara, M., Ferrez, J.-A., Ramaioli, M., Liebling, T.M., 2005. Granular Matter 7, 119.

Richter, A., Nikrityuk, P.A., 2013. Powder Technol. 249, 463.

Rong, L., Dong, K., Yu, A., 2013. Chem. Eng. Sci. 99, 44–58.

Rosendahl, L., 2000. Appl. Math. Modell. 24, 11.

Salikov, V., Antonyuk, S., Heinrich, S., Sutkar, V.S., Deen, N.G., Kuipers, J., 2015. Powder Technol. 270 (Part B), 622.

Sanjeevi, S.K.P., Padding, J.T., 2017. J. Fluid Mech. 820.

Sanjeevi, S.K.P., Kuipers, J.A.M., Padding, J.T., 2018. Int. J. Multiphase Flow 106, 325–337.

Son, S.R., Kim, S.D., 2006. Ind. Eng. Chem. Res. 45, 2689.

Stukowski, A., 2010. Modell. Simul. Mater. Sci. Eng. 18, 015012.

Tran-Cong, S., Gay, M., Michaelides, E.E., 2004. Powder Technol. 139, 21.

Tsuji, Y., Kawaguchi, T., Tanaka, T., 1993. Powder Technol. 77, 79.

Vega, C., Lago, S., 1994. Comput. Chem. (Oxford) 18, 55.

Vollmari, K., Jaseviius, R., Kruggel-Emden, H., 2016. Powder Technol. 291, 506.

Vorobiev, N., Becker, A., Kruggel-Emden, H., Panahi, A., Levendis, Y.A., Schiemann, M., 2017. Fuel 210, 107.

Warnecke, R., 2000. Biomass Bioenergy 18, 489.

Werther, J., 2000. Fluidized-Bed Reactors. Wiley-VCH Verlag.

Williams, P.T., Williams, E.A., 1999. J. Anal. Appl. Pyrol. 51, 107.

Woytiuk, K., Campbell, W., Gerspacher, R., Evitts, R., Phoenix, A., 2017. Renew. Energy 101, 409.

Xu, B., Yu, A., 1997. Chem. Eng. Sci. 52, 2785.

Xue, Y., Kelkar, A., Bai, X., 2016. Fuel 166, 227.

Zastawny, M., Mallouppas, G., Zhao, F., van Wachem, B., 2012. Int. J. Multiph. Flow 39, 227.

Zhao, J., Shan, T., 2013. Powder Technol. 239, 248.

Zhu, H., Zhou, Z., Yang, R., Yu, A., 2007. Chem. Eng. Sci. 62, 3378.

Zhu, H., Zhou, Z., Yang, R., Yu, A., 2008. Chem. Eng. Sci. 63, 5728.